MAXIMIZING DETECTION RANGE IN LIDAR SYSTEMS THROUGH THE USE OF GATED PHOTOMULTIPLIER TUBES

Chandler A. Slater
Advisor: Richard C. Zimmerman Ph.D.
Old Dominion University Department of Ocean and Earth Sciences

Abstract

Oceanographic optical lidar applications seek to overcome limitations inherent in passive ocean color retrievals. While current experimental lidar systems offer depth-resolved signals, they often fall short in capturing the entire euphotic zone. This study introduces a novel approach to enhance the detection range of shipborne oceanographic lidar systems by integrating gated photomultiplier tubes (PMTs) with a multi-channel high digital amplification digitizer board. This strategy aims to leverage the dynamic range of gated PMTs to extend surface ocean detection. Laboratory measurements and optical calibrations were conducted to characterize system timing. Subsequently, the system was tested in a pool to assess signal return in a clear water scenario and demonstrate the efficacy of gated PMTs. The results indicate the gated PMT approach extends the detection range of oceanographic lidar systems by capturing nearfield and far field sections separately and stitching them into a continuous profile.

Introduction

The advent of ocean color remote sensing has fundamentally transformed our understanding of primary productivity and surface dynamics in the ocean. The introduction of the Coastal Zone Color Scanner and more than 25-year continuous time series initiated with the SeaWIFS satellite mission have enabled global coverage of various geophysical ocean properties. However, despite these advancements, passive radiometric retrieval methods encounter several limitations. These include solely capturing the surface-weighted optically integrated signal, aggregating signal contributions from both above and below the water surface, and failing to provide information regarding the vertical distribution of ocean parameters(Collister et al., 2018; Gordon, 1997; Gordon & McCluney, 1975; Hill et al., 2013; Hostetler et al., 2018; Jamet et al., 2019). To address these challenges, the utilization of oceanographic profiling lidar has been pursued with the aim of overcoming the inherent constraints in ocean color retrievals.

Lidar, known as light detection and ranging, is an active source remote sensing technique that utilizes the time of flight of a pulsed laser to determine the position of an object that induced a backscattered signal. The advent of highspeed digitizers has allowed for the capture of the full waveform of backscattered light from a laser emission as a function of time. Through correction of recorded time of flight, accounting for the speed of light within the sample medium, accurate range detection is achieved. This capability enables the determination of information regarding the vertical distribution of particles and the internal structure of the surface ocean. (J. H. Churnside et al., 2001; Collister et al., 2018; Hill et al., 2013; Hoge et al., 1988; Hostetler et al., 2018; Lee et al., 2013).

Applications of these systems have been used on experimental bases across a host of platforms and applications. Zooplankton vertical migration, fish school detection, thin scattering layers and chlorophyll concentrations have all been studied using spaceborne, airborne, and shipborne techniques (Behrenfeld et al., 2013; J.

Churnside & Donaghay, 2009, 2009; J. H. Churnside, 2001; Collister et al., 2018; Zhou et al., 2022). The depth-resolved measurements of the technique allow for vertical profiles of ocean optical properties, such as particulate backscattering B_{bp}, the diffuse light attenuation coefficient K_d, and the depolarization ratio [δ] at the emitted wavelengths to be measured. Using a polarized laser source and polarizing beam slitter allows the backscattered pulse to be parsed into co- and cross-polarized signals with respect to the polarization of the original emitted source. This additional signal allows for investigations into particle composition. The polarization of a backscattered signal allows the differentiation between non depolarizing spherical particles such as bubbles and depolarizing non spherical particles such as phytoplankton (Hostetler et al., 2018a). The use of the ratio of depolarization has been utilized to determine particle composition (J. Churnside et al., 2013; J. H. Churnside, 2008; Collister et al., 2020, 2022; Liu et al., 2019; Vasilkov et al., 2001). The use of the polarized signals has also extended the detection range of bottom structures and non-depolarizing objects by lowering the dynamic range necessary for the digitizer (Vasilkov et al., 2001).

The experimental applications of the oceanographic lidar systems provided depth resolved optical measurements to 40-50 meters in optically clear Case I waters and less in Case II waters (Chen et al., 2022; J. H. Churnside et al., 2001; Collister et al., 2018; Zhou et al., 2022). This range corresponds to approximately 50% of the euphotic zone or about 2 optical depths ($\zeta=K_d z$). However, despite their capacity for depth-resolved retrieval, the depth penetration of these systems remains similar to that of integrated ocean color retrievals (10% isolume or 2.3ζ). The inability to detect signals down to the full euphotic depth (4.6ζ or ~100 meters in clear oceanic waters) hinders the accurate determination of the vertical structure of the surface ocean. Consequently, significant features such as the deep chlorophyll maximum observed in oligotrophic subtropical gyres and summer polar seas, which could serve as potent drivers of primary production in these otherwise low chlorophyll regions, remain uncaptured (J. Churnside & Donaghay, 2009; Hill et al., 2013; Hill & Zimmerman, 2010; Jamet et al., 2019; Zimmerman et al., 2013). This limitation stems from the inadequate dynamic range available in digitizers, which prevents them from capturing the full waveform of the signal, ranging from high-energy surface reflections to low signal-to-noise returns from depths exceeding 3ζ (J. H. Churnside et al., 2001; Vasilkov et al., 2001).

To address this problem a novel approach to oceanographic optical profiling lidar applications has been developed by the Bio-Optical Research Group (BORG) at Old Dominion University. This approach incorporates range-gated photomultiplier tubes (PMTs) for both co- and cross-polarized signals, integrated with a customized data acquisition and controller board from Nalu Scientific LLC. These cutting-edge electronics enable the PMTs to capture signals at various intervals of the laser pulse, utilizing low gain and open gate settings for near-field measurements, and high gain and late opening gate settings for deeper measurements. This strategic adjustment maximizes the dynamic range of the board and extends the system's detection capability into the water column. The digitizer board boasts a 2 GHz sampling rate and 8 data channels, enabling digital amplification of the co- and cross-polarized inputs to enhance the board's dynamic range. The primary focus of this study evaluates the potential of gated PMTs to extend the detection range of oceanographic lidar systems. This is achieved through in-lab and pool testing, aimed at quantifying the signal return for depth-resolved optical properties.

Methods

Laser System

The lidar system utilized in this study is an upgraded version of the system used and described in (Collister et al., 2018a) thus forward referred to as “Beast” The Beast system is equipped with a Quantel Viron diode-pumped Q-switched Nd: YAG laser 1064 nm frequency doubled to 532 nm. The laser emits a linearly polarized 25 mJ pulse with a pulse width of 10 ns and a beam divergence of <2 mrad. The beam is directed through a beam expanding telescope and subsequently oriented through a pair of steering mirrors (Thorlabs Model NB1-K13) to orient the beam parallel to the optical detectors and to reduce the divergence to 0.5 mrad.

Detection Optics

The detection optics for receiving the backscattered pulse were positioned biaxially adjacent to the laser source. The backscattered light passes through a bandpass interference filter to eliminate background light outside the laser emission wavelength (Semrock LL01-532-12.5: 2.0 nm FWHM bandwidth; 12.5 mm diameter), the signal is then directed through an anti-reflection coated polarizing beam splitter cube (CVI PBS-532-050; 1000:1 Tp/Ts extinction ratio; Tp > 95%, Rs > 99.9% 12.5mm) to separate co-polarized and cross-polarized signals. The PMTs are oriented parallel to ensure equal detection footprints and to package the system within the waterproof housing. Due to the polarization orientation of the laser and detection optics, the cross-polarized signal bypasses the polarizing beam splitter. In contrast, the co-polarized signal undergoes redirection, being deflected 90° off-axis to a non-reflection coated steering mirror (Thorlabs MRA25-E02) before reaching the co-polarized PMT. To account for the increased travel distance incurred by the co-polarized signal due to the mirror, the cross-polarized signal PMT is adjusted backward, ensuring equal distance to the viewing window and a uniform field of view for both detectors. A summary of instrument characteristics and specifications are listed in (Table 1.).

Packaging

The instrument was designed to sample the surface ocean from above-water shipboard applications as well as in-water moorings. Recognizing the diverse conditions encountered in these sampling environments, a robust waterproof housing was developed. The waterproof housing is composed of anodized aluminum tube with machined and anodized aluminum end caps. A 7.62 cm diameter acrylic viewing window for the laser and detection optics is recessed in the forward-facing endcap. Wet-mate bulkhead connectors provide power and data communication and storage from the systems to the operators PC laptop running the capture software.

Data Acquisition Board and Triggering

The co-polarized and cross-polarized signals were recorded digitally using 8-channel 12-bit resolution Ocean Lidar Environmental Aquatic Sampling digitizer (OLEAS) sampling at 2 GHz developed by Nalu Scientific Inc. The digitizing board also controls the operation of the laser and detection optics during samplings with 2 auxiliary channels. The laser trigger of the first auxiliary channel triggers the board to begin its sampling process and open the PMTs dependent on when the operator set the timing in the data capture software. The 2.4V auxiliary signal to trigger the PMTs is fed to a bias Tee where it is supplemented with a 2V baseline voltage to increase the signal to 4V to trigger the TTL gate opening for the PMTs. A separate I2C communication with a small Adafruit board (Adafruit MCP4728) that controls the gain of the PMTs.

Software Optimization

The unique application of the OLEAS board with gated PMTs required custom data capture and real-time visualization software to operate the system and capture data simultaneously. Two python scripts were created by Nalu Scientific and tested in the BORG laboratory to optimize the timing of the system and the ability to capture and visualize data reliably to the operator. The capture script for each system controls the laser pulse, PMT gate opening, PMT gain control, as well as data acquisition and saving to the connected PC laptop. The script has several settings that allow the user to manually input commands for the timing for the optics. Tests were conducted within the lab by firing the system at a Spectralon target mounted on a 4 m rail system. Settings were adjusted to begin collection at low gain settings and an open PMT gate to capture near field data without blinding the optics or saturating the digitizer. The gate and gain settings were then increased for the gate to miss the initial flash of the acrylic viewing window and open to view much lower backscattered signals farther downrange.

Lab Testing and Calibration

The gate opening percentage as a function of time elapsed was quantified for each setting. The system was placed on the fitting on a sliding rail and a Spectralon plaque was placed 50 cm downrange of the systems. The pulsed laser was blocked, and a continuous wavelength (CW) laser was directed to the Spectralon plaque in front of the PMT window opening. The system was set to sample regularly, cycling through gate settings. The average of each gate setting was then taken and normalized to determine the percentage of PMT power during the gate opening process. This information was utilized in post-processing to identify when the signals from the gate settings were at optimal PMT power for signal processing.

Pool Testing

Once the settings were optimized for near field detection within 4m, the system was tested in the Old Dominion University Student Recreational Center Pool. This test's purpose was twofold: 1) to continue to adjust the gate and gain settings to optimize the timing of the systems detectors 2) To investigate the systems behavior and detection range in a clear water environment similar to that of the Case I oligotrophic ocean.

For the pool test the instruments were positioned to fire along the length of the pool 21.34 m from the back wall. Identical captures were conducted targeting the black tiles of the back wall marking the swimming lanes of the competition pool. This was done to minimize the specular reflection off the back wall. The known length of the pool and the position of the systems to the back wall was also used to validate the range corrected signal return of the system. The systems were then oriented to fire obliquely across the pool to increase the available detection range within the confines of the pool geometry.

To obtain a comprehensive optical profile of the pools water, instruments measuring inherent and apparent optical properties were also deployed during the test. The instruments consisted of an ac-S (WET LABS) in-situ spectrophotometers measuring the absorption coefficient (a) and beam attenuation coefficient (c) for total non-water contribution (a_{gp} and c_{gp}). A Hydroscat-6 (HOBI Labs) backscatter meter measuring particulate backscattering coefficient (b_{bp}). A laser in-situ scattering transmissometer (LISST-100) was also used to measure the volume scattering function (VSF), beam attenuation (c), as well as particle distribution of spherical particles (SSD) and random shape particles (RSD). Two custom hyperspectral radiometers (HyperRAD) developed in the BORG lab were deployed 1 meter vertically distant and collected downwelling irradiance as a function depth for the calculation of K_d. The optical

properties captured by the instruments were used to characterize the lidar return signal.

Signal Processing

During the data collection process the OLEAS board cycled through gate and gain settings set by the user in the capture python script. The capture processed collected shots at each gain and gate setting before cycling to the next iteration of settings set by the software. There was a 3 second pause between settings to allow for the PMTs to settle. Data logging was triggered by the OLEAS board as well as the trigger for the laser and PMT gate and gains. All values for the triggering were saved as well to files created by the digitizer. For the Beast system the laser Q switch triggering had an inherent 175 ± 0.1 µsecond delay from when the trigger signal was sent to the laser before it fired. The OLEAS board was set to start recording 174.8 µseconds after the trigger signal was sent. Due to the inherent jitter of the Q-switched laser the fluctuation in the signal made an unreliable signal for determining time-zero for ranging. Additionally, the use of the gated PMTs in gate settings that open the PMTs post initial flash did not allow for determination of time-zero for later gate captures. To address this a photodiode was placed in front of the laser independent of the PMT collection optics. This signal rise of the photodiode was used as an indicator for time-zero for the range correction of the signal.

The underwater deployment in the pool allowed the range to be calculated by converting the sample number of the OLEAS board to nanoseconds (1 sample = 781.85 picoseconds) multiplying by the speed of light in water (0.225 m ns^{-1}) then by dividing the signal by two to account for the round trip for each photon.

Each set of shots taken at their respective gain settings underwent averaging and subsequent stitching to enhance the effective signal-to-noise ratio and extend the detection range of the system. The stitching process involved rescaling each averaged waveform to match the profiles measured at the highest gain settings, thereby identifying overlapping regions of the scaled waveforms. These overlapping signals served as the reference for slicing each waveform, ensuring selection of the waveform with the highest signal-to-noise ratio without saturation (see Figure 1). This procedure continued with respect to the lowest gain setting as the initial flash with stitching occurring by selecting signals from increasing gate and gain signals until a continuous waveform was complete with the highest possible SN ratio.

The continuous waveform profile of the returned signal was then smoothed using a nearest neighbor approach to mitigate noise introduced by higher gain settings from the digitizer in order to achieve a more consistent profile of the optical return of the signal. The system attenuation coefficient (K_{sys}) was then calculated by using the slope of the decay in the return signal using methods of (Kovalev & Eichinger, 2004).

$$K_{\text{sys}} = -\frac{1}{2}\frac{d}{dR}\ln\left[P_r(R)R^2\right] \qquad (1)$$

Where R was the range along the beam, and the multiplication of the return signal by R^2 corrects for the decrease in solid angle subtended by the detector with range. Regions of the signal that were contaminated by the specular reflection of the viewing window and off the pool back wall were excluded in the analysis. The return for the systems were log transformed and normalized to compare. with other systems published for calculations of K_{sys}.

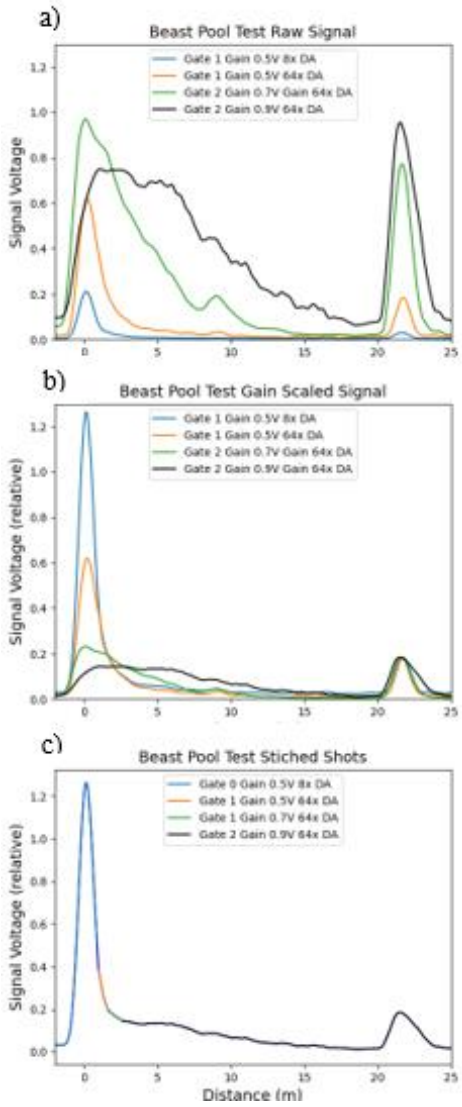

Figure 1. Lidar signal processing workflow. a) Averaged raw return signals from each respective gate, gain, and digital amplification (DA) setting collected during the pool test and selected for stitching. The signal quality at each setting as well as the flat-topped peak for signal behavior at the digitizer saturation threshold of 0.87 V is shown. Lower initial flash amplitude for later gain settings indicates that the gating of the PMT past the first peak works to dampen the initial flash except for slight ringing from the PMT caused by the bright initial flash off the window captured by the near field gate settings. b) The scaled lidar signals transformed to match a single PMT gain and digital amplification setting to match relative amplitude of the return signal. c) stitched lidar signal created by indexing overlaps of arrays and selecting signals with the highest S:N ratio to create a continuous return.

Results

The lidar return signal for the pool deployment was measured for the response in the clear water conditions experienced during an in-water deployment. The full width half max FWHM of the signal peaks were 14.84 ns for the initial flash and 35.38 ns for the back wall return for the shots taken along the pool length. For shots taken in the oblique position the initial flash was 17.19 ns for the first peak and 38.28 ns (Figure 2.). The K_{sys} was consistent from the viewing window until the back wall of the pool for the along pool measurement but displayed a larger drop in signal magnitude when the signal approached 20 m for the oblique angle shots. The K_{sys} were identical for both returns and were an order of magnitude higher than measurements of a_{pg} or c_{pg}, with c_{pg}. Although all measured inherent and apparent optical properties of the water approached pure water thresholds (Pope & Fry, 1997).

The back wall measured by the systems occurred at 22.104 ± 0.497 m and 25.137± 0. 0.203 m for the Beast system positions when the systems were pointed shooting along the measured pool length (Figure 2a). The range gating allowed the measurement of the optical backscatter from the decay of the signal to the pool wall 21.336m along the length and 25 m for the diagonal position (Figure 2b). The signal after the return from the back wall is due to multiple scattering occurring within the pool that continues for 87ns before returning to noise level.

Table 1. lidar system component summary

Lidar System Parameters	
Parameter	Value
Laser Source	
Laser	Frequency doubled diode pumped Nd-YAG
Pulse rate	10Hz
Wavelength	532 nm
Pulse energy	25.4 mJ
Pulse width	4 ns FWHM
Beam diameter	1 cm
Beam divergence	<2 mrad
Polarization	Vertical Linear Polarization
Receiver optics	
Interference Filter	
Diameter	12.5 mm
Filter bandwidth	2 nm FWHM
Attenuation filter	0.01 (OD?)
Polarizing beamsplitter	
Extinction ratio (Tp: Ts)	>1000:1
Transmission P-Polarization	> 95%
Reflectance S-Polarization (Rs)	> 99.9%
Detector	
Type	Photomultiplier tube
Collection mode	Current
Rise Time	0.57 ns
System geometry	
Field of view (full angle)	7 (above-water)
Detector configuration	Biaxial
optical axis offset	3.5 cm
Range to overlap	29 cm (above-water)
Data acquisition	
Sampling rate	2 Gsamples s^-1 channel^-1
Resolution	12 bit
Channels	8

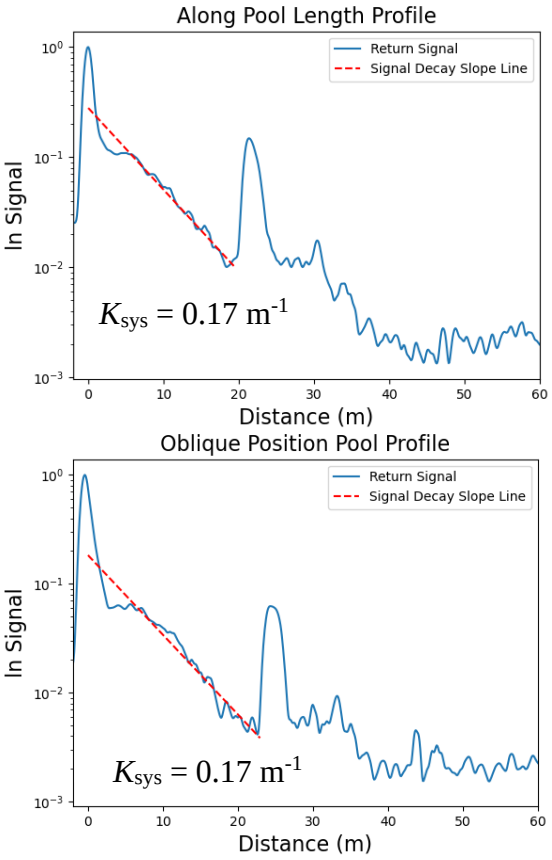

Figure 2**.** Lidar return of the stitched signal profile from the Beast lidar system positioned firing a) along the length of the pool with the system placed 21.336m from the back wall. b) The system positioned to fire diagonally across the pool to maximize used range within the confines of the pool geometry. The system attenuation was calculated from T0 to the distance to the back wall.

Discussion

Pool Deployment

The deployment of the system in a clear pool water environment provided valuable insights into their characteristics. The signal showed consistent K_{sys} for both positions as to be expected in clear homogeneous pool water. Range recording and alignment during data processing introduced approximately 0.5m of uncertainty in determining scattering locations. The uncertainty in distances to the back wall stemmed from return signals saturating the digitizer, exceeding the saturation threshold of 0.87 (Figure 1. a) as seen with the significantly large FWHM of the back wall peaks in (Figure 2). The specular reflection from the back wall should ideally exhibit a Gaussian distribution with a full width at half maximum (FWHM) matching the laser pulse width (Table 1).

The saturation of the digitizer from the return signal off the back wall indicates sufficient power for the system to capture optical properties from distances beyond the pool's geometry. This was reinforced by the sustained multiple scattering input to the digitizer, which persists for approximately one third of the total signal after the flash.

The initial flash also offered insights into the reaction and recovery of the PMTs at their lowest gain setting during an in-water deployment. Such a response cannot be replicated in a lab setting, where the in-air return only yields a Gaussian response to the window. Therefore, only in-water testing with sufficient downrange geometry, such as in a competition swimming pool, can effectively investigate the initial flash and decay trail of the signal as photons return to the detector throughout the water column.

The small dip in the signal after the flash is characteristic of PMTs (Jiang et al., 2012). This ringing response by the PMTs in clear water will likely be exacerbated in turbid coastal waters that cause higher amplitude surface returns modeled in (Zimmerman et al., 2013) and observed in (Collister et al. 2018). The return from the clear pool test has allowed this problem to be identified for future signal processing.

PMT Gating

Gating the PMTs enabled characterization of the full length of the pool. Without the range gating the detection of the full decay of the signal to the pool back wall in both orientation for Beast would not have been possible. The digitizer limit to 0.87V for this system requires the initial flash to be sampled at the lowest PMT gain setting. To address this, gating the PMTs beyond the initial pulse and flash off the viewing window enables setting higher gain settings to observe scattering returning from farther downrange without saturating the digitizer or blinding the PMTs.

References

Behrenfeld, M. J., Hu, Y., Hostetler, C. A., Dall'Olmo, G., Rodier, S. D., Hair, J. W., & Trepte, C. R. (2013). Space-based lidar measurements of global ocean carbon stocks: SPACE LIDAR PLANKTON MEASUREMENTS. *Geophysical Research Letters*, *40*(16), 4355–4360. https://doi.org/10.1002/grl.50816

Chen, P., Liu, D., & Jamet, C. (2022). LiDAR Remote Sensing for Vertical Distribution of Seawater Optical Properties and Chlorophyll-a From the East China Sea to the South China Sea. *IEEE Transactions on Geoscience and Remote Sensing*, *60*, 1–21. https://doi.org/10.1109/TGRS.2022.3174230

Churnside, J., & Donaghay, P. (2009). Thin scattering layers observed by airborne lidar. *Ices Journal of Marine Science - ICES J MAR SCI*, *66*, 778–789. https://doi.org/10.1093/icesjms/fsp029

Churnside, J. H. (2001). Airborne lidar for fisheries applications. *Optical Engineering*, *40*(3), 406. https://doi.org/10.1117/1.1348000

Churnside, J. H. (2008). Polarization effects on oceanographic lidar. *Optics Express*, *16*(2), 1196. https://doi.org/10.1364/OE.16.001196

Churnside, J. H., Wilson, J. J., & Tatarskii, V. V. (2001). Airborne lidar for fisheries applications. *Optical Engineering*, *40*(3), 406–414. https://doi.org/10.1117/1.1348000

Churnside, J., Mccarty, B., & Lu, X. (2013). Subsurface Ocean Signals from an Orbiting Polarization Lidar. *Remote Sensing, Vol. 5, Issue 7, Pp. 3457-3475*, *5*, 3457–3475. https://doi.org/10.3390/rs5073457

Collister, B. L., Zimmerman, R. C., Hill, V. J., Sukenik, C. I., & Balch, W. M. (2020). Polarized lidar and ocean particles: Insights from a mesoscale coccolithophore bloom. *Applied Optics*, *59*(15), 4650–4662. https://doi.org/10.1364/AO.389845

Collister, B. L., Zimmerman, R. C., Sukenik, C. I., Balch, W. M., & Hill, V. J. (2022). The influence of particle concentration and bulk characteristics on polarized oceanographic lidar measurements. *Limnology and Oceanography*, *67*(6), 1374–1387. https://doi.org/10.1002/lno.12088

Collister, B. L., Zimmerman, R. C., Sukenik, C. I., Hill, V. J., & Balch, W. M. (2018). Remote sensing of optical characteristics and particle distributions of the upper ocean using shipboard lidar. *Remote Sensing of Environment*, *215*, 85–96. https://doi.org/10.1016/j.rse.2018.05.032

Gordon, H. R. (1997). Atmospheric correction of ocean color imagery in the Earth Observing System era. *Journal of Geophysical Research: Atmospheres*, *102*(D14), 17081–17106. https://doi.org/10.1029/96JD02443

Gordon, H. R., & McCluney, W. R. (1975). Estimation of the Depth of Sunlight Penetration in the Sea for Remote Sensing. *Applied Optics*, *14*(2), 413–416. https://doi.org/10.1364/AO.14.000413

Hill, V. J., Matrai, P. A., Olson, E., Suttles, S., Steele, M., Codispoti, L. A., & Zimmerman, R. C. (2013). Synthesis of integrated primary production in the Arctic Ocean: II. *In situ* and remotely sensed estimates. *Progress in Oceanography*, *110*, 107–125. https://doi.org/10.1016/j.pocean.2012.11.005

Hill, V. J., & Zimmerman, R. C. (2010). Estimates of primary production by remote sensing in the Arctic Ocean: Assessment of accuracy with passive and active sensors. *Deep Sea Research Part I: Oceanographic Research Papers*, *57*(10), 1243–1254. https://doi.org/10.1016/j.dsr.2010.06.011

Hoge, F. E., Wright, C. W., Krabill, W. B., Buntzen, R. R., Gilbert, G. D., Swift, R. N., Yungel, J. K., & Berry, R. E. (1988). Airborne lidar detection of subsurface oceanic scattering layers. *Applied Optics*, *27*(19), 3969–3977. https://doi.org/10.1364/AO.27.003969

Hostetler, C. A., Behrenfeld, M. J., Hu, Y., Hair, J. W., & Schulien, J. A. (2018). Spaceborne Lidar in the Study of Marine Systems. *Annual Review of Marine Science*, *10*(1), 121–147. https://doi.org/10.1146/annurev-marine-121916-063335

Jamet, C., Ibrahim, A., Ahmad, Z., Angelini, F., Babin, M., Behrenfeld, M. J., Boss, E., Cairns, B., Churnside, J., Chowdhary, J., Davis, A. B., Dionisi, D., Duforêt-Gaurier, L., Franz, B., Frouin, R., Gao, M., Gray, D., Hasekamp, O., He, X., … Zhai, P.-W. (2019). Going Beyond Standard Ocean Color Observations: Lidar and Polarimetry. *Frontiers in Marine Science*, *6*, 251. https://doi.org/10.3389/fmars.2019.00251

Jiang, W.-Q., Gu, S.-D., Joseph, J., Liu, D.-W., Luk, K.-B., Steiner, H., Wang, Z., & Wu, Q. (2012). Suppressing ringing caused by large photomultiplier tube signals. *Chinese Physics C*, *36*(3), 235–240. https://doi.org/10.1088/1674-1137/36/3/008

Kovalev, V. A., & Eichinger, W. E. (2004). *Elastic Lidar: Theory, Practice, and Analysis Methods*. John Wiley & Sons.

Lee, J. H., Churnside, J. H., Marchbanks, R. D., Donaghay, P. L., & Sullivan, J. M. (2013). Oceanographic lidar profiles compared with estimates from in situ optical measurements. *Applied Optics*, *52*(4), 786–794. https://doi.org/10.1364/AO.52.000786

Liu, Q., Cui, X., Chen, W., Liu, C., Bai, J., Zhang, Y., Zhou, Y., Liu, Z., Xu, P., Che, H., & Liu, D. (2019). A semianalytic Monte Carlo radiative transfer model for polarized oceanic lidar: Experiment-based comparisons and multiple scattering effects analyses. *Journal of Quantitative Spectroscopy and Radiative Transfer*, *237*, 106638. https://doi.org/10.1016/j.jqsrt.2019.106638

Pope, R. M., & Fry, E. S. (1997). Absorption spectrum (380–700 nm) of pure water. II. Integrating cavity measurements. *Applied Optics*, *36*(33), 8710–8723. https://doi.org/10.1364/AO.36.008710

Vasilkov, A., Yury, G., Gureev, B., Hoge, F., Swift, R., & Wright, C. (2001). Airborne Polarized Lidar Detection of Scattering Layers in the Ocean. *Applied Optics*, *40*, 4353–4364. https://doi.org/10.1364/AO.40.004353

Zhou, Y., Chen, Y., Zhao, H., Jamet, C., Dionisi, D., Chami, M., Di Girolamo, P., Churnside, J. H., Malinka, A., Zhao, H., Qiu, D., Cui, T., Liu, Q., Chen, Y., Phongphattarawat, S., Wang, N., Chen, S., Chen, P., Yao, Z., … Liu, D. (2022). Shipborne oceanic high-spectral-resolution lidar for accurate estimation of seawater depth-resolved optical properties. *Light: Science & Applications*, *11*(1), Article 1. https://doi.org/10.1038/s41377-022-00951-0

Zimmerman, R. C., Sukenik, C. I., & Hill, V. J. (2013). 18—Subsea LIDAR systems. In J. Watson & O. Zielinski (Eds.), *Subsea Optics and Imaging* (pp. 471–488e). Woodhead Publishing. https://doi.org/10.1533/9780857093523.3.471